

1 **Introducing the MISR Level 2 Near Real-Time Aerosol Product**

2
3
4
5
6
7
8
9
10
11
12
13
14
15
16
17
18
19
20
21
22
23
24
25
26
27
28

Marcin. L. Witek¹, Michael J. Garay¹, David J. Diner¹, Michael A. Bull¹, Felix C. Seidel¹, Abigail M. Nastan¹, and Earl G. Hansen¹

¹Jet Propulsion Laboratory, California Institute of Technology, 4800 Oak Grove Drive, Pasadena, CA 91109, USA

Abstract

Atmospheric aerosols are an important element of Earth's climate system, and have significant impacts on the environment and on human health. Global aerosol modeling has been increasingly used for operational forecasting and as support to decision making. For example, aerosol analyses and forecasts are routinely used to provide air quality information and alerts in both civilian and military applications. The growing demand for operational aerosol forecasting calls for additional observational data that can be assimilated into models to improve model accuracy and predictive skill. These factors have motivated the development, testing, and release of a new near real-time (NRT) level 2 (L2) aerosol product from the Multi-angle Imaging SpectroRadiometer (MISR) instrument on NASA's Terra platform. The NRT product capitalizes on the unique attributes of the MISR aerosol retrieval approach and product contents, such as reliable aerosol optical depth as well as aerosol microphysical information. Several modifications are described that allow for rapid product generation within a three-hour window following acquisition of the satellite observations. Implications for the product quality and consistency are discussed as compared to the current operational L2 MISR aerosol product. Several ways of implementing additional use-specific retrieval screenings are also highlighted.

@ 2021. California Institute of Technology. Government sponsorship acknowledged

29 **1. Introduction**

30

31 Atmospheric aerosols have for long been recognized to influence the climate, environment, and
32 human health (e.g., IPCC, 2013; Lelieveld et al., 2015; Shindell et al., 2013; Turnock et al.,
33 2020). They also affect satellite remote sensing of important geophysical parameters such as
34 ocean color (e.g., Frouin et al., 2019; Gordon, 1997) or greenhouse gas abundance (Butz et al.,
35 2009; Frankenberg et al., 2012; Houweling et al., 2005). Aerosol particles and their properties
36 have been extensively studied in-situ and remotely: from the ground, in the air, and from space.
37 These observational data vary in spatial and temporal coverage, but usually only offer
38 snapshots of local conditions. Since atmospheric aerosols have a life cycle ranging from hours
39 to days, numerical modeling of their emission, transport, and deposition has filled the coverage
40 gaps and extended our understanding of their global impacts. This has given rise to a number of
41 global aerosol reanalyses (Buchard et al., 2017; Gelaro et al., 2017; Inness et al., 2013, 2019;
42 Lynch et al., 2016; Randles et al., 2017; Rienecker et al., 2011) that provide a long-range,
43 gridded, and internally consistent outlook on aerosol burdens around the world. Furthermore,
44 global aerosol modeling has been increasingly used for operational forecasting (e.g., Xian et al.,
45 2019) and as support to decision making, for example in air quality alerts and in non-civilian
46 applications (Liu et al., 2007).

47 The growing demand for consistent gridded aerosol products has been driving
48 development and steady improvement of numerical predictions. For example, the International
49 Cooperation for Aerosol Prediction initiative was founded in 2010 (Benedetti et al., 2011; Reid et
50 al., 2011), with one of its goals being the development of global multi-model aerosol forecasting
51 ensemble for basic research and operational use (Xian et al., 2019). Still, models suffer from
52 often poorly resolved aerosol emissions and sinks and can be affected by errors in the
53 underlying meteorology. As a result, systematic and sampling-related biases in aerosol fields
54 are often found between model simulations and satellite observations (e.g., Buchard et al.,
55 2015; Colarco et al., 2010; Lamarque et al., 2013; Zhang and Reid, 2009). An effective way to
56 mitigate some of these problems is by assimilating aerosol observations into numerical models
57 (e.g., Bocquet et al., 2015; Fu et al., 2017; Sekiyama et al., 2010; Di Tomaso et al., 2017;
58 Werner et al., 2019; Zhang et al., 2008). Satellite observations of aerosol optical and
59 microphysical properties are inseparable from these data assimilation activities as they offer the
60 necessary data volume, near-global coverage, and frequent repeat cycle. However, an often-
61 considerable latency for generating science-quality “standard” satellite products (8 to 40 hours)
62 renders them unsuitable for operational forecasting. This has led to the development of aerosol

63 products within the time frame required by modeling centers, usually three hours from satellite
64 overpass. A number of near real-time (NRT) products has emerged.

65 One example of a platform that provides users with NRT satellite products and imagery
66 is NASA's Land, Atmosphere Near real-time Capability for EOS (LANCE) project
67 (<https://earthdata.nasa.gov/earth-observation-data/near-real-time>). A range of instruments
68 deliver various Level 1 (L1) and Level 2 (L2) data products
69 ([https://earthdata.nasa.gov/collaborate/open-data-services-and-software/data-information-](https://earthdata.nasa.gov/collaborate/open-data-services-and-software/data-information-policy/data-levels)
70 [policy/data-levels](https://earthdata.nasa.gov/collaborate/open-data-services-and-software/data-information-policy/data-levels)), including radiances, land surface properties, and atmospheric
71 thermodynamics and composition within three hours from satellite observation. NRT aerosol
72 products are currently available from the Moderate Resolution Imaging Spectroradiometer
73 (MODIS), Ozone Monitoring Instrument (OMI), and Visible Infrared Imaging Radiometer Suite
74 (VIIRS). NASA's Multi-angle Imaging SpectroRadiometer (MISR) currently provides NRT
75 radiance and cloud motion vector products. The purpose of this paper is to introduce a new
76 MISR NRT L2 aerosol product available within LANCE.

77 This paper is organized as follows. Section 2 and 3 provide brief descriptions of the
78 MISR instrument and the data processing sequence, respectively. Section 4 first outlines the
79 cloud identification methods employed in the MISR aerosol algorithm and then describes
80 algorithmic modifications introduced in the NRT processing. Adjustments to cloud and retrieval
81 screening parameters and their implications are discussed. The global distributions of the NRT
82 product [and comparisons of total and fractional AODs with the standard aerosol product](#) are
83 [presented](#) in Section 5. Section 6 provides a summary.

Deleted: analyzed

84

85 **2. MISR instrument and aerosol data product**

86

87 The MISR instrument flies aboard the NASA Earth Observing System (EOS) Terra satellite,
88 launched in December 1999 to a sun-synchronous descending polar orbit, at an orbital altitude
89 of 705 km, an orbital period of 99 minutes, and an equatorial crossing time of 10:30 a.m. local
90 time. MISR makes 14.56 orbits per day with a repetition cycle (revisit) of 16 days. The orbit
91 tracks are georeferenced to a fixed set of 233 ground paths. With a cross-track swath of about
92 380 km, total Earth coverage is obtained every 9 days at the equator and every 2 days at high
93 latitudes.

94 MISR contains nine pushbroom cameras with viewing angles at the Earth's surface
95 ranging from 0° (nadir) to +/- 70.5° oriented along the direction of the flight track. A point on the
96 ground is imaged by all nine cameras in approximately 7 minutes. The cameras make

98 observations of reflected solar radiance in four spectral bands, centered at 446 (blue), 558
99 (green), 672 (red), and 866 (near-infrared) nm. The spatial resolution depends on the camera
100 and wavelength. The red band has a full 275 m resolution in all cameras. The other three
101 spectral channels are averaged onboard to a 1.1 km resolution in global-mode operation (Diner
102 et al., 1998), with the exception of the nadir camera which preserves the full 275 m resolution in
103 all spectral channels. See <https://misr.jpl.nasa.gov/Mission/> for more details.

104 MISR employs two processing pathways for aerosol retrievals, one for observations over
105 land (Martonchik et al., 2009), and another for dark water (DW) (Kalashnikova et al., 2013),
106 which applies over deep oceans, seas, and lakes. Previous versions of the MISR aerosol
107 product were extensively validated over the years (e.g., Kahn et al., 2010; Kahn and Gaitley,
108 2015; Kalashnikova et al., 2013; Shi et al., 2014; Witek et al., 2013) showing high retrieval
109 quality over land and ocean.

110 The current operational version of the MISR aerosol product, designated as version 23
111 (V23), was released publicly in June 2018. It introduced multiple algorithmic, data product, and
112 data usability improvements (Garay et al., 2020; Witek et al., 2018a, 2018b). V23 provides
113 aerosol information with a spatial resolution of 4.4 km x 4.4 km packaged in NetCDF-4 format.
114 Initial validation efforts showed that V23 retrievals are more accurate than previous versions,
115 with most pronounced improvements in the DW algorithm (Garay et al., 2020). V23 retrievals
116 over oceans were extensively validated by Witek et al. (2019), indicating excellent agreement
117 with ground-based observations. Other V23 Aerosol Optical Depth (AOD) evaluation efforts
118 show similar results (e.g., Choi et al., 2019; Sayer et al., 2020; Si et al., 2020; Sogacheva et al.,
119 2020). A first regional insight into retrieved particle properties from the MISR V23 aerosol
120 product shows that MISR generally captures the distinct spatial and temporal features of aerosol
121 type in East Asia (Tao et al., 2020). Furthermore, V23 has greatly improved the quality of
122 reported AOD uncertainties, which now realistically represent retrieval errors (Sayer et al., 2020;
123 Witek et al., 2019). This is especially relevant as pixel-level retrieval uncertainties are very
124 important for satellite data assimilation, which is being increasingly used in aerosol modeling
125 studies (Lynch et al., 2016; Shi et al., 2011, 2013; Zhang and Reid, 2010). MISR data and
126 related documentation can be obtained from: <https://asdc.larc.nasa.gov/project/MISR>.

127

128 **3. NRT latency and data description**

129

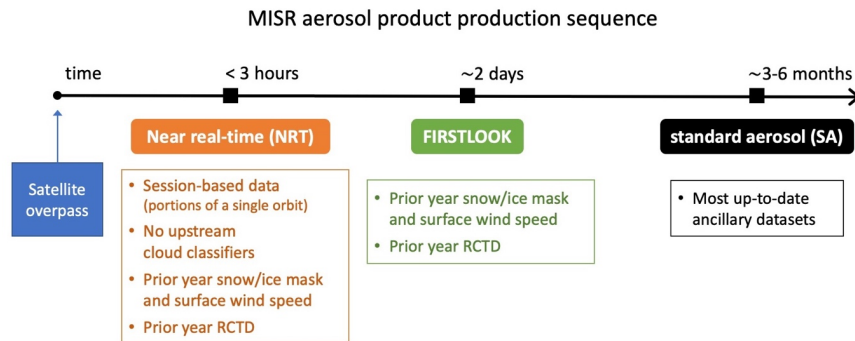
130 MISR currently provides several L1 and L2 near real-time (NRT) radiance and cloud motion
131 vector products (<https://earthdata.nasa.gov/earth-observation-data/near-real-time/download-nrt->

132 [data/misr-nrt](#)). All MISR NRT processing is based on Level 0 data downlinked in observational
133 sessions. These session-based files, representing portions of a single MISR orbit, usually cover
134 between 10 to 50 minutes of observations, as compared to the full orbit period of 98.9 minutes.
135 This session-based processing is necessary to allow for the fast product delivery required for
136 NRT applications.

137 The new NRT L2 aerosol product file content, described in Data Product Specification
138 (https://asdc.larc.nasa.gov/documents/misr/DPS_AEROSOL_NRT_V023.20210430.pdf), is
139 equivalent to the standard aerosol product (Garay et al., 2020). The NRT L2 aerosol product file
140 name convention is:

141 MISR_AM1_AS_AEROSOL_T{yyyymmddHHMMSS}_P{ppp}_O{oooooo}_F13_0023.nc, where
142 'yyyy', 'mm', and 'dd' are the year, month, and day, and 'HH', 'MM' and 'SS' are the hour,
143 minute, and seconds, respectively. Furthermore, {ppp} is the three-digit path identifier (between
144 001 and 233) and {oooooo} is the six-digit orbit number. The NRT L2 aerosol product files are
145 available for download within three hours of acquisition at NASA's Atmospheric Science Data
146 Center (ASDC) (<https://asdc.larc.nasa.gov/project/MISR>).

147 For clarity, it is important to distinguish between the three different MISR L2 aerosol
148 products: NRT, FIRSTLOOK, and standard aerosol (SA) product (see Figure 1). NRT is
149 generated within a three-hour time interval after acquisition and uses the same ancillary inputs
150 as FIRSTLOOK. These include the monthly gridded (1.0 degree) snow/ice mask and surface
151 wind speed from the Terrestrial Atmospheric and Surface Climatology (TASC) database and the
152 seasonal Radiometric Camera-by-camera Threshold Dataset (RCTD) (Diner et al., 1999a). Both
153 NRT and FIRSTLOOK utilize TASC and RCTD datasets from the current month/season in the
154 prior year. The FIRSTLOOK product is generated within two days from acquisition and includes
155 cloud classification parameters obtained from the L1 and L2 cloud products. The SA product is
156 available after final processing is performed on a seasonal basis and within three months past
157 the end of the season, which results in a 3–6-month latency. The final processing utilizes the
158 most recent snow/ice and wind speed data.



159
 160 Figure 1 Schematic showing MISR aerosol product delivery timeline. Snow/ice mask and surface wind speed data are monthly
 161 averages. RCTD stands for Radiometric Camera-by-camera Threshold Dataset. MISR final production (SA) is processed on a
 162 seasonal cycle and is often delayed one to three months past the end of each season, which results in up to 6-month latency.
 163

164 **4. Cloud screening in the NRT MISR aerosol product**

165
 166 **4.1. Cloud identification**

167
 168 Identification of cloudy pixels is a critical element of all satellite aerosol remote sensing
 169 algorithms. MISR employs several cloud identification strategies which can be loosely split into
 170 two groups: the first group relies on cloud classifiers previously generated with MISR Level 2
 171 Cloud Detection and Classification algorithm (Diner et al., 1999b), and the second group
 172 includes build-in tests that are internal to the aerosol retrieval algorithm (Diner et al., 2008).
 173

174 **4.1.1. Upstream cloud classifiers**

175
 176 The operational MISR aerosol algorithm relies on a range of external input datasets that are
 177 either static—for example, a monthly wind speed climatology—or that need to be generated
 178 prior to aerosol retrievals in upstream processing. A notable example of such external inputs to
 179 the SA and FIRSTLOOK algorithms are cloud classification parameters obtained from the MISR
 180 L2 cloud product. An important implication of this dependency is that aerosol processing needs
 181 to wait for the cloud product to be generated, creating a time lag that is prohibitive for NRT
 182 applications. Typically, the L2 cloud product is generated within about 18 hours of overpass,

183 and the MISR L2 FIRSTLOOK aerosol processing is completed within about 2 days. In order to
184 produce an L2 aerosol product within an about three-hour time frame, the algorithm needs to
185 operate without the upstream cloud classifiers.

186 Two specific L2 cloud classification parameters utilized in FIRSTLOOK and SA aerosol
187 processing are the MISR Stereoscopically-Derived Cloud Mask (SDCM) and the Angular
188 Signature Cloud Mask (ASCM) (Diner et al., 1999b; Girolamo and Davies, 1994). In addition to
189 these L2 products, the Radiometric Camera-by-camera Cloud Mask (RCCM) (Diner et al.,
190 1999a; Girolamo and Davies, 1995) retrieved in L1B processing is also employed. All three
191 parameters are reported at 1.1 km x 1.1 km resolution. It should be noted that RCCM also
192 serves as an input to the algorithm that generates SDCM and ASCM, indicating that these
193 parameters are not independent.

194 In the FIRSTLOOK and SA algorithm, the RCCM, SDCM, and ASCM cloud masks are
195 used together to determine whether a particular 1.1 km x 1.1 km subregion is clear or cloudy.
196 The implication is that if any of the 9 MISR cameras is designated as cloudy in a subregion, this
197 subregion is excluded from aerosol retrieval. The clear/cloudy decision logic depends on the
198 underlying surface type, assigned into three categories: land, water, and snow/ice. Generally, a
199 “clear” outcome is favored over the two most frequently used surface types, land and water,
200 assigning a subregion as cloudy only if the RCCM and SDCM masks indicate a cloud. The logic
201 is considerably more conservative over snow/ice surfaces due to difficulties in distinguishing
202 clouds from the underlying bright features. Details of the cloud mask decision logic over different
203 surface types can be found in Diner et al. (2008).

204 Analyzing three months of V23 L2 SA product (March, April, May, 2020) indicates that
205 the cloud masks along with the brightness test (see 4.1.2) lead to screening of about 50% of
206 retrievals. As such, they have the largest impact on identifying and removing pixels where
207 clouds might be present. These masks and decision pathways, however, have their deficiencies
208 and additional checks were put in place to further decrease the frequency of cloud-
209 contaminated aerosol retrievals.

210

211 4.1.2. **Built-in cloud detection methods**

212

213 In addition to the cloud masks retrieved in the L1B processing (RCCM) and from the L2 Cloud
214 Detection and Classification algorithm (SDCM, ASCM), the MISR aerosol retrieval algorithm
215 relies on three internal tests to further identify cloudy pixels that might have escaped earlier
216 detection. These are (1) the *brightness test*, (2) the *angle-to-angle smoothness test*, and (3) the

Deleted: Build

218 *angle-to-angle correlation test*. Details of these tests can be found in Diner et al. (2008) or Witek
219 et al. (2013), but a short summary is provided here for completeness.

220 The brightness test is employed to identify clouds that lacked sufficient texture to be
221 picked up by SDCM. For each surface type a fixed threshold is adopted on measured
222 bidirectional reflectance factors (BRFs), and when exceeded in all spectral bands for at least
223 one camera, it renders a subregion unsuitable for aerosol retrieval. The thresholds are set to
224 1.0, 0.5, and 0.5 for snow/ice, land, and water surfaces, respectively. The value of 1.0 means
225 that the brightness test is effectively turned off over snow/ice. Furthermore, the brightness test
226 does not override subregions that were identified as clear by RCCM.

227 The angular smoothness test checks for unusually large variations in the measured
228 equivalent reflectances as a function of camera angle, the premise being that in the absence of
229 artifacts or subpixel clouds, the measured radiance should change smoothly from camera to
230 camera. The test is achieved by fitting a polynomial to equivalent reflectances, separately for aft
231 (+nadir) and forward (+nadir) cameras and each spectral band, and checking if the goodness of
232 fit metric (definition in Diner et al., 2008) exceeds a threshold. If in at least one case the test
233 fails, the subregion is eliminated.

234 Finally, the angle-to-angle correlation test also investigates radiance smoothness and
235 correlation between camera angles, which makes it conceptually similar to the angular
236 smoothness test, but instead utilizes high-resolution information from the red spectral band. It
237 uses 4 x 4 arrays of the 275m spatial resolution red band equivalent reflectances in each 1.1 km
238 x 1.1 km subregion. The test then evaluates spatial variability within the 4 x 4 array for each
239 camera and compares it to a variability within a camera-average template. Variances,
240 covariances, and normalized cross-correlations are calculated (see Diner et al., (2008) for
241 details). If the variability within a camera deviates considerably from the average, this camera
242 might have sub-pixel clouds or other contaminants, and as a result the subregion is excluded
243 from aerosol retrievals.

244 In the three months of data analyzed in this study (March, April, May 2020), the relative
245 occurrence of retrieval screening due the above-mentioned internal tests are about 4.0% and
246 0.1% for the correlation and smoothness tests, respectively. These statistics come from
247 analyzing the output field *Aerosol_Retrieval_Screening_Flags* and as such they do not
248 represent the absolute rates of success of each individual test. That is because the tests are
249 performed in a sequential order and if one of them fails, tests that are next in sequence are not
250 performed. For SA product generation, the order is: upstream cloud mask described in 4.1.1,
251 the brightness test, the correlation test, and the smoothness test. For example, the correlation

252 test is only performed on pixels that already passed the upstream cloud tests as well as the
253 brightness test. Additionally, the brightness test does not have its own flag in the
254 *Aerosol_Retrieval_Screening_Flags* output but is grouped together with the upstream cloud
255 classifiers.

256

257 **4.2. Retrieval screening using regional cloud parameters**

258

259 Methods described in section 4.1 focus on identifying and excluding cloudy 1.1 km x 1.1 km
260 subregions from the aerosol retrieval process. The retrieval region consists of 16 (4 x 4)
261 subregions. These methods are highly effective at removing cloud-contaminated pixels, but
262 since they rely on MISR visible wavelengths they might miss certain cloud signatures more
263 easily detected in the infrared spectrum (e.g., Gao et al., 1993). For example, MODIS routinely
264 uses its reflective and emissive infrared channels to detect optically thin cirrus clouds
265 (Ackerman et al., 2010; Levy et al., 2013). As a result, MISR cloud detection methods
266 occasionally fail, which leads to visible outliers in retrieved AODs (Witek et al., 2018b). For that
267 reason, an additional set of screenings is applied in an effort to eliminate such unusually high
268 AOD retrievals (Garay et al., 2020). Two of these additional methods look at overall cloudiness
269 in the retrieval region (consisting of 4 x 4 subregions) as well as in a larger area consisting of 3
270 x 3 regions (12 x 12 subregions). The Cloud Screening Parameter (CSP) represents the fraction
271 of clear grid cells within a region, whereas Cloud Screening Parameter Neighbor 3x3 (CSP9) is
272 similar to CSP but for the larger area. If CSP is below 0.7 and CSP9 below 0.5, the retrieval is
273 not reported in the final product intended for most users. However, it is still included in the
274 product's AUXILIARY subcategory and annotated with the term "Raw" to indicate that the
275 product has not undergone recommended quality screenings.

276

277 **4.3. Adjusting cloud screening thresholds**

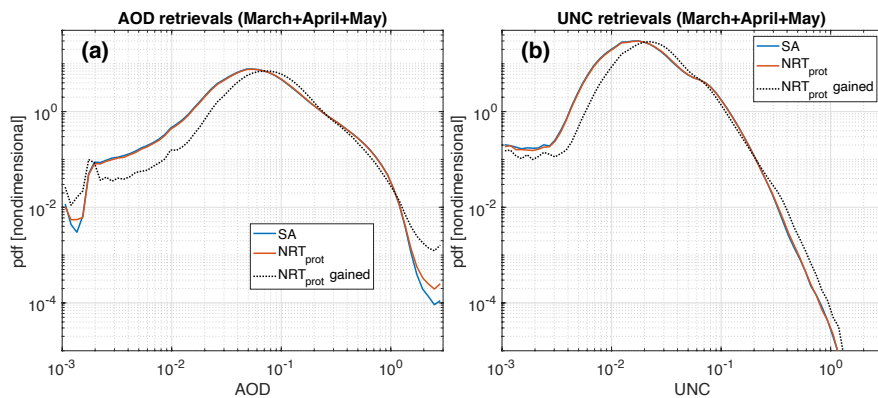
278

279 **4.3.1. Performance of the prototype NRT product**

280

281 This subsection presents results and analysis of prototype NRT aerosol retrievals. These are
282 obtained prior to any threshold and screening adjustments included in the final version of the
283 product. To differentiate between the final and the prototype NRT products, the latter is denoted
284 as NRT_{prot} .

285 As mentioned in the previous section, the NRT processing cannot rely on the cloud
 286 masks generated in the L1 and L2 cloud products, namely the RCCM, SDCM, and ASCM. This
 287 implies that potentially less screening of cloudy subregions would be applied, increasing the
 288 probability of cloud contamination in aerosol retrievals. However, some of the burden of cloud
 289 identification is picked up by the built-in cloud tests described in section 4.1.2. The frequency of
 290 these tests identifying cloudy pixels increases in NRT processing in comparison to standard
 291 processing, in large part mitigating the negative consequences resulting from the lack of the
 292 upstream cloud masks. This is well evidenced by examining the normalized probability density
 293 functions (*pdfs*) of AOD from spring 2020 (Figure 2). The SA (red) and NRT_{prot} (blue) lines are
 294 very similar, indicating that the built-in cloud tests substitute to a significant extent for the
 295 missing upstream cloud masks in generating the NRT_{prot} product. The largest difference occurs
 296 in the high-AOD range, suggesting that NRT_{prot} has more retrievals in this regime. The black
 297 dotted line shows a *pdf* of the NRT_{prot} AOD retrievals that do not have a matching SA retrieval.
 298 This is labeled as “NRT_{prot} gained” as it represents additional retrievals obtained in NRT
 299 processing due to the lack of external cloud masks. The “NRT_{prot} gained” *pdf* is clearly shifted
 300 towards higher AODs, confirming that the NRT_{prot} processing tends to retrieve higher AODs in
 301 places where SA is not available.

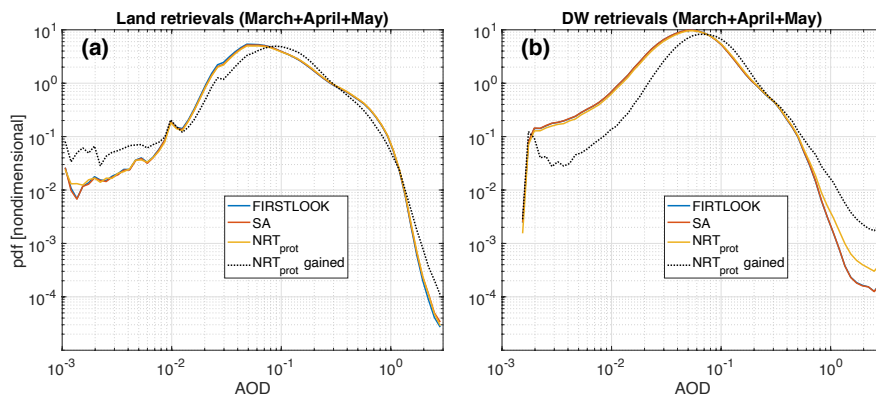


302 Figure 2 (a) AOD normalized probability density functions from SA, prototype NRT, and prototype NRT retrievals that do not
 303 have a matching SA equivalent (labeled as NRT_{prot} gained); (b) same as in (a) but for retrieved AOD uncertainties (UNC). Data
 304 statistics for AODs are provided in Table 1.
 305

306 Figure 3 shows *pdfs* of AOD but with retrievals separated between DW (Fig. 3a) and
 307 land (Fig. 3b). These *pdfs* indicate that the retrievals over oceans are the main source of

308 increased frequency of high-AODs in the NRT_{prot} product. The *pdfs* over land are virtually
 309 unchanged, including a slightly flattened but still relatively comparable distribution of the “NRT_{prot}
 310 gained” retrievals (Fig. 3b). The additional statistics of the data presented in Figs. 2 and 3,
 311 including the retrieval count, the mean AOD, and the geometric mean AOD, which is better
 312 suited for log-normal distributions of AOD (Sayer and Knobelspiess, 2019), are provided in
 313 Table 1. Note that the number of NRT_{prot} gained is not the same as the number of NRT_{prot} minus
 314 SA. This is because some SA retrievals do not have their NRT_{prot} equivalent, making the SA
 315 count larger than it would have been otherwise.

316 In the 3-month period analyzed in this study (March, April, May, 2020), the NRT_{prot}
 317 processing leads to about 6.4% more retrievals than SA (see Table 1). 5.5 million NRT_{prot}
 318 retrievals do not have a matching SA retrieval (NRT gained), and the majority of them (67%) are
 319 DW retrievals. The overall geometric means are almost identical in SA and NRT_{prot}, although
 320 small variations in this statistic are seen in DW and land categories. The NRT gained have
 321 visibly higher mean and geometric mean values, the increase coming mainly from DW
 322 retrievals. These basic statistics warrant a further look at the NRT_{prot} performance over DW.



323
 324 Figure 3 AOD pdfs for land (a) and DW (b) retrievals, respectively. Data statistics are provided in Table 1.

	All retrievals			DW			Land		
	SA	NRT _{prot}	NRT _{prot} gained	SA	NRT _{prot}	NRT _{prot} gained	SA	NRT _{prot}	NRT _{prot} gained
$N (\times 10^6)$	49.7	52.9	5.5	27.6	30.7	3.7	22.1	22.2	1.8

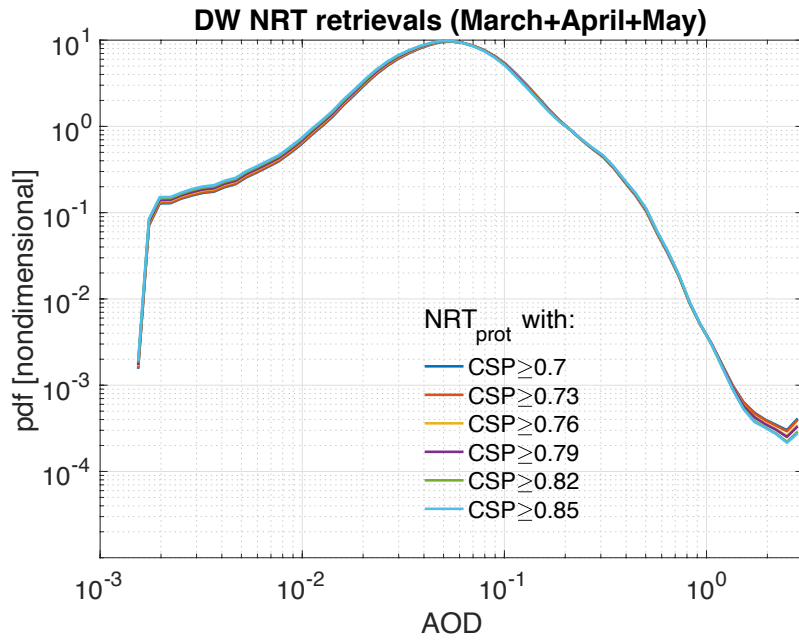
<i>mean</i>	0.168	0.169	0.171	0.111	0.115	0.146	0.240	0.243	0.224
<i>geomean</i>	0.111	0.112	0.122	0.083	0.085	0.106	0.160	0.162	0.161

Table 1 Additional statistics for the data presented in Figs. 2 and 3 (statistic for FIRSTLOOK not shown). NRT gained stands for the prototype NRT retrievals that do not have a matching SA equivalent; geomean stands for the geometric mean AOD.

4.3.2. Sensitivity to CSP and CSP9 thresholds in DW retrievals

One way to screen potentially cloud-contaminated high-AOD retrievals is to adjust thresholds on CSP and CSP9 parameters (Garay et al., 2020). This is furthermore justified by the fact that in the absence of RCCM, SDCM, and ASCM in NRT_{prot} processing, fewer cloudy subregions are identified in a retrieval area and consequently CSP and CSP9 have by default lower values. This argument provides strong justification for investigating sensitivity to increased CSP and CSP9 thresholds in the NRT_{prot} processing.

The SA product uses the thresholds of CSP=0.7 and CSP9=0.5 (Garay et al., 2020); when the values of CSP and CSP9 are below these thresholds in a retrieval region, the aerosol retrieval is removed from the data field recommended for users. Figure 4 and Table 2 show *pdfs* and AOD statistics for different thresholds of CSP and CSP9 parameters in the NRT_{prot} product over dark water surfaces. There are only minor changes in the *pdfs* when the thresholds are increased, including in the high-AOD regime. The mean and geometric mean decrease gradually but slowly; even at the highest considered thresholds (0.85 for CSP and 0.75 for CSP9) these statistics are still above the SA values. At the same time the number of passing NRT_{prot} retrievals decreases considerably faster, with almost 19% of retrievals lost when the highest thresholds are used. These results indicate that adjusting CSP and CSP9 thresholds is not an effective strategy to constraining NRT_{prot} retrievals.



347
 348 Figure 4 Prototype NRT AOD pdfs over dark water surfaces from spring 2020 obtained with different CSP and CSP9 cloud-
 349 screening thresholds. Data statistics are provided in Table 2.

$N (\times 10^6)$	30.7	30.1 (-1.9%)	28.4 (-7.4%)	27.7 (-9.8%)	25.9 (-15.6%)	24.9 (-18.9%)	SA 27.6
CSP	≥ 0.7	≥ 0.73	≥ 0.76	≥ 0.79	≥ 0.82	≥ 0.85	
CSP9	≥ 0.5	≥ 0.55	≥ 0.6	≥ 0.65	≥ 0.7	≥ 0.75	
mean	0.1151 ± 0.1200	0.1149 ± 0.1199	0.1145 ± 0.1190	0.1144 ± 0.1191	0.1142 ± 0.1185	0.1143 ± 0.1189	0.1110 ± 0.1079
geomean	0.0850	0.0847	0.0841	0.0839	0.0834	0.0832	0.0826

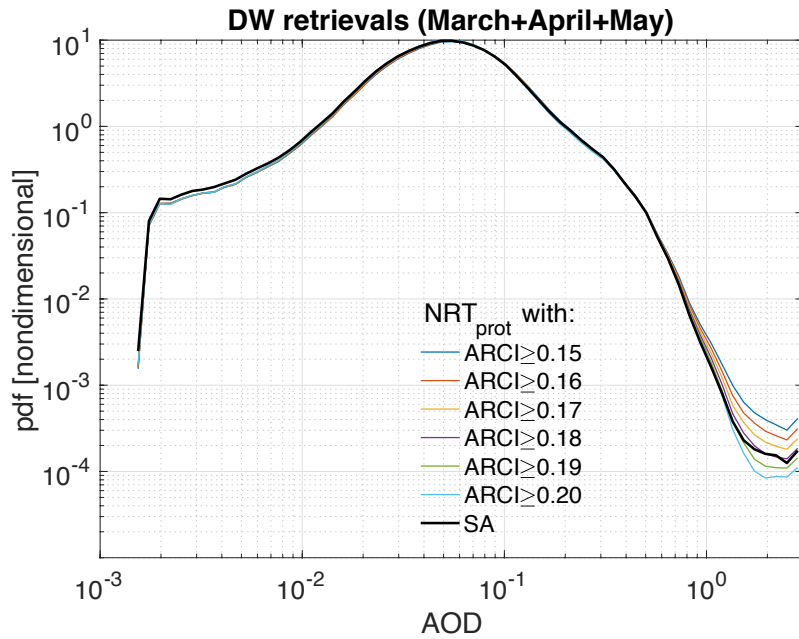
350 Table 2 Additional statistics for the data presented in Fig. 4. Values for CSP and CSP9 indicate their corresponding thresholds for
 351 screening AOD retrievals. The arithmetic mean values are accompanied by their respective \pm one standard deviations.

352
 353 **4.3.3. Sensitivity to ARCI threshold in DW retrievals**

354

355 V23 of the MISR aerosol product introduced a new parameter, called the aerosol retrieval
356 confidence index (ARCI), that is used to screen high-AOD retrieval outliers caused by cloud
357 contamination and other factors (Witek et al., 2018b). ARCI, defined only for DW retrievals,
358 proved to be an efficient metric at filtering out potentially cloud-contaminated AOD retrievals. In
359 standard processing, retrievals with $ARCI < 0.15$ are removed from the recommended user
360 field, but are retained in the AUXILIARY group. The 0.15 threshold is well supported through
361 statistical analysis (Witek et al., 2018b), although some erroneous AODs still pass this
362 screening method, suggesting that increasing this threshold might be beneficial in NRT
363 processing.

364 Figure 5 and Table 3 show *pdfs* and AOD statistics for different thresholds of ARCI in the
365 NRT_{prot} product. In this case the differences between ARCI thresholds are quite noticeable,
366 especially in the high-AOD range of retrievals. Increasing the ARCI threshold to 0.2 leads to a
367 loss of about 11% of NRT_{prot} DW retrievals, but the resulting mean and geometric mean are
368 lower than the SA values. At the same time, the absolute number of NRT_{prot} DW retrievals (27.4
369 million) is still comparable to the number of SA DW retrievals (27.6 million). The *pdfs* and the
370 statistics suggest that increasing the NRT_{prot} ARCI threshold from 0.15 to 0.18 leads to a
371 product that has similar characteristics to SA.



372
 373 Figure 5 Prototype NRT AOD pdfs from spring 2020 obtained with different ARCI thresholds. Data statistic are provided in Table
 374 3.

$N (\times 10^6)$	30.7	30.0 (-2.2%)	29.4 (-4.3%)	28.7 (-6.5%)	28.0 (-8.6%)	27.4 (-10.8%)	SA 27.6
ARCI	≥ 0.15	≥ 0.16	≥ 0.17	≥ 0.18	≥ 0.19	≥ 0.20	
mean	0.1151 ± 0.1200	0.1137 ± 0.1157	0.1124 ± 0.1122	0.1112 ± 0.1094	0.1100 ± 0.1070	0.1090 ± 0.1051	0.1110 ± 0.1079
geomean	0.0850	0.0842	0.0835	0.0828	0.0821	0.0813	0.0826

375 Table 3 Additional statistic for the data presented in Fig. 5.

376

377 4.3.4. Recommendation for NRT processing

378

379 The statistical analyses presented in the previous sections indicate that the lack of RCCM,
 380 SDCM, and ASCM in NRT processing has negative consequences on the product, especially by

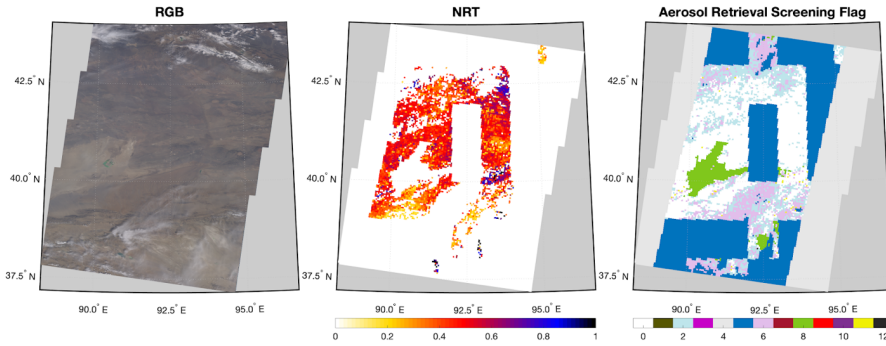
381 allowing more, potentially cloud-contaminated, high-AOD DW retrievals to pass screening
382 criteria. Adjusting build-in cloud screening thresholds on CSP and CSP9 brings only limited
383 benefits at the cost of losing a considerable percentage of retrievals. However, the ARCI
384 threshold adjustments result in much closer statistical correspondence between the NRT_{prot} and
385 standard AOD retrievals. For that reason, a revised ARCI threshold of 0.18 is implemented in
386 NRT processing. Since the unscreened retrievals, as well as the ARCI parameter, are also
387 provided in the AUXILIARY group of the product, users are encouraged to experiment with their
388 own thresholds which might prove more beneficial in specific applications or geographic areas.
389

390 **4.4. Cloud/clear decision logic over snow/ice**

391
392 In section 4.1.1 the impact of upstream cloud classifiers in standard processing—namely the
393 RCCM, SDCM, and ASCM—on the subregion’s cloud/clear designation was briefly described.
394 The decision pathway depends on the underlying surface type, which can be either land, water,
395 or snow/ice. Over land and water, the “cloud” outcome is only obtained when both RCCM and
396 SDCM designate the subregion as cloudy. In the absence of RCCM and SDCM the default
397 outcome is “clear”. Over snow/ice, however, the logic is more restrictive and favors the “cloudy”
398 designation (Diner et al., 2008). Specifically, when the upstream cloud classifiers are not
399 available, the subregion designation is set to “cloudy” by default. This has important implications
400 on aerosol retrievals in areas where snow and ice occur seasonally.

401 The snow/ice surface mask, unlike land and water, is not static and changes every
402 month. Furthermore, the snow/ice mask input to MISR aerosol processing has a 1.0-degree
403 horizontal resolution, which is re-gridded to a 1.1 km resolution corresponding to the resolution
404 of MISR subregion. In FIRSTLOOK processing, the snow/ice mask from the same month but in
405 the previous year is used. The final SA processing is performed when the current year’s monthly
406 snow/ice mask becomes available. The NRT processing, similarly to FIRSTLOOK, relies on the
407 previous year’s snow/ice mask. Additionally, given the lack of upstream cloud classifiers, the
408 snow/ice areas are designated as “cloudy” for aerosol retrieval purposes. This is well visualized
409 in Figure 6 which shows the visible image and the corresponding maps of AOD and Aerosol
410 Retrieval Screening Flag in the NRT processing. The dark blue color (index 5) denotes cloudy
411 regions determined using the snow/ice cloud logic. The box-like nature of the excluded areas is
412 associated with the coarse resolution of the snow/ice mask (1.0 degree). The previous year’s
413 mask might also not be representative of the current conditions on the ground. It is worth noting
414 that the FIRSTLOOK product often suffers from the same exclusion rules as NRT. This is

415 because of the strict clear/cloud logic over snow/ice surfaces which favors the cloudy outcome;
 416 in the case shown in Fig. 6 the AOD gaps in FIRSTLOOK (not shown) look very similar to the
 417 NRT product.



418
 419 *Figure 6 Example of snow/ice masking in NRT AOD retrievals. (Left) Visible image of the retrieval area. (Center) Corresponding*
 420 *NRT AOD retrievals. (Right) NRT Aerosol Retrieval Screening Flag for the same area; the dark blue color denotes regions*
 421 *designated as cloudy.*

422 Several attempts have been made by the MISR science team to improve NRT aerosol
 423 retrievals in snow/ice covered areas. However, identifying and isolating snow-covered surfaces
 424 in the absence of upstream cloud classifiers proves very challenging. The quality of aerosol
 425 retrievals is often negatively affected in such conditions. For that reason, and in an attempt to
 426 eliminate as many NRT AOD outliers as possible, the current snow/ice logic is retained in the
 427 NRT aerosol processing.

428

429 **5. NRT and SA product comparisons,**

430

431 **5.1. Total AOD**

432

433 In this section, geographic distributions of MISR AOD retrievals from SA and NRT products are
 434 analyzed. The datasets encompass three months, March, April, and May of 2020. The NRT
 435 retrievals are screened with the revised ARCI threshold of 0.18 as suggested in section 4.3.4.

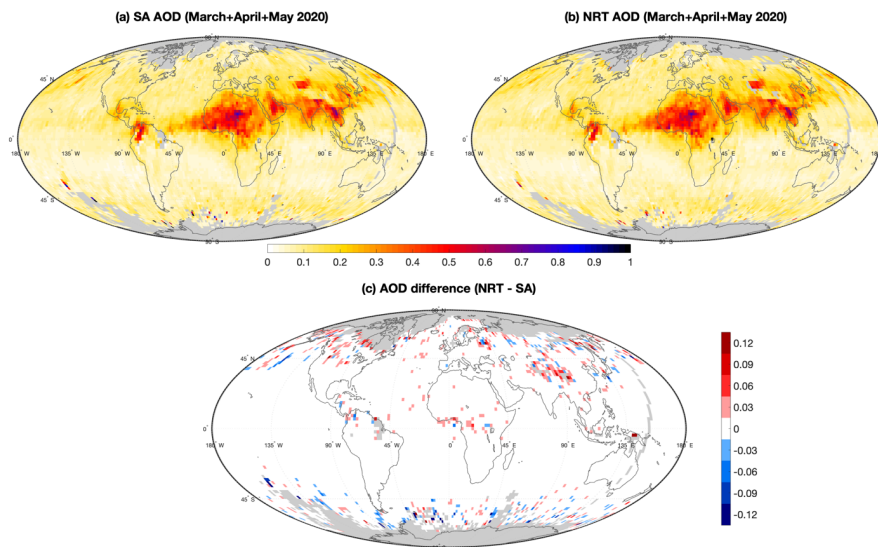
436 The spatial overlap of the SA and NRT data is achieved using an intersect of the X_Dim and
 437 Y_Dim fields in the two data products.

Deleted: differences

Deleted: AOD

440 Figure 7 shows the global distributions of geometric mean AOD from the (a) SA and (b)
441 NRT products. The retrievals are gridded at 2-by-2-degree spatial resolution. Fig. 7c shows the
442 AOD difference between the two products (NRT – SA).

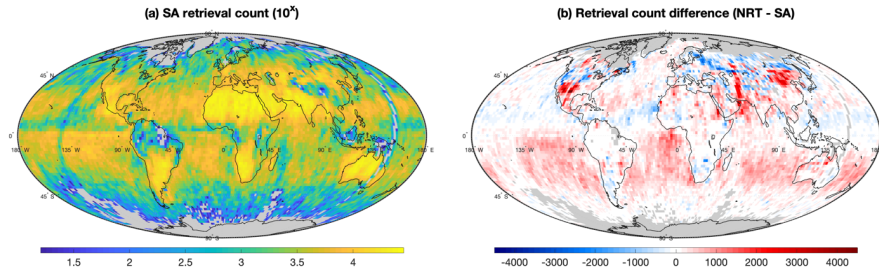
443 The largest AOD differences are seen in areas with climatologically high cloud cover,
444 especially over the Southern Ocean, and over land in areas where potential snow cover could
445 be an issue. Over the Southern Ocean the SA AODs are predominantly higher than the NRT
446 AODs. This is due to the increased ARCI threshold in NRT (0.18 vs. 0.15 in SA) which brings in
447 more aggressive screening of cloud-contaminated retrievals (Witek et al., 2018b). Over land,
448 where the ARCI parameter is not available, the gridded NRT AODs tend to be higher than the
449 SA AODs, which is in part related to the differences in snow/ice mask between the two
450 products. Still, the AOD differences in Fig. 7c are rather small and reflect sampling issues rather
451 than any systematic deficiencies in NRT processing. At the same time the lack of cloud
452 classifiers in NRT does not adversely affect AOD distributions, which is consistent with the
453 statistical analysis presented in section 4.2.3.



454
455 *Figure 7 (a) Global distribution of SA AOD geometric mean values across March, April, and May of 2020 on a 2-by-2-degree*
456 *spatial resolution; (b) same as in (a) but for NRT AOD; and (c) AOD difference between SA and NRT. Grid points with less than 15*
457 *retrievals are excluded.*

458 5.2. Retrieval yields

459 Figure 8 complements Fig. 7 by showing (a) the SA retrieval count distribution as well as (b) the
460 retrieval count difference between the SA and NRT products.



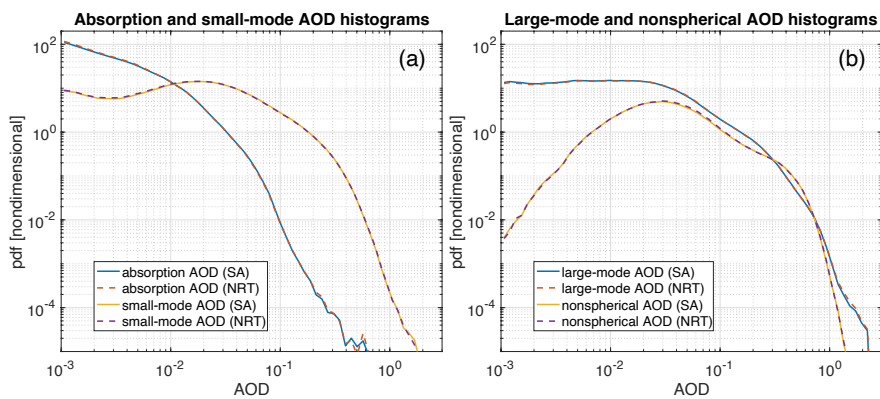
461
462 Figure 8 (a) Decimal logarithm of the retrieval count from the SA product in March, April, and May of 2020; (b) retrieval count
463 difference between SA and NRT. Presented values are gridded at 2-by-2-degree spatial resolution and grid points with less than
464 15 retrievals are excluded.

465 The highest number of retrievals is found over the subtropical continents where the
466 cloud cover is usually the smallest. Over the subtropical oceans in the Southern Hemisphere the
467 NRT retrieval counts are typically higher than in SA, which results from the absence of upstream
468 cloud classifiers in NRT processing and subsequently fewer subregions being excluded as
469 cloudy. Note that this increase in retrieval count caused by the lack of cloud classifiers is not
470 compensated by the increased ARCI threshold in NRT processing ($ARCI \geq 0.18$), which always
471 reduces the number of retrievals when compared to the default SA threshold ($ARCI \geq 0.15$). The
472 lack of hemispheric symmetry in this case is likely due to the seasonal variability (only months in
473 northern spring are analyzed here). Over land the lack of upstream cloud classifiers also results
474 in higher number of NRT retrievals in certain regions, but the surface type exclusion rules
475 reverse this pattern, especially at higher latitudes. The conservative cloud logic over snow/ice
476 surfaces in NRT processing often results in the lower number of NRT retrievals in the high
477 latitudes of the northern hemisphere.

478 A metric relevant to the potential use of the NRT product in data assimilation is the
479 retrieval yield per model grid point. The retrieval yield can be measured as, for example, the
480 number of $1^\circ \times 1^\circ$ grid cells that have at least 15 valid satellite retrievals in them. From this
481 perspective, the NRT product has a retrieval yield that is about 0.7% higher than the SA
482 product, based on the three months of data analyzed in this study.

483 5.3. Fractional AOD

486 MISR's multi-angle retrieval approach enables characterization of aerosol optical and
 487 microphysical properties, such as fractional AODs associated with particle absorption,
 488 nonsphericity, and size (see e.g., Kahn and Gaitley, 2015). This attribute of the MISR SA
 489 product has been applied to many climate and air quality studies and inclusion of this capability
 490 in the NRT product would benefit data assimilation for numerical prediction of atmospheric
 491 aerosols (Benedetti et al., 2018). Consequently, this section provides preliminary statistical
 492 comparisons of the SA and NRT absorption AOD along with small-mode, large-mode, and
 493 nonspherical AOD. The results shown in Fig. 9 indicate that the probability density functions of
 494 these aerosol properties in the NRT product are statistically equivalent to the SA product. This
 495 assessment reaffirms the consistency of the NRT and SA products. Future studies will examine
 496 geographic and statistical differences and other particle properties in more detail.



497 *Figure 9 Normalized probability density functions for select MISR particle property retrievals in March, April, and May 2020.*
 498 *Solid lines represent SA retrievals and dashed represent NRT retrievals. (a) absorption AOD and small-mode AOD retrievals; (b)*
 499 *large-mode AOD and nonspherical AOD retrievals. The differences between the SA and NRT products are negligible.*

501
 502 **6. Summary**

503
 504 The MISR V23 aerosol product, publicly available since mid-2018, is a high-resolution state-of-
 505 the-art data product from NASA's Terra flagship mission. V23 AOD retrievals have remarkable
 506 accuracy compared against ground-based observations (Garay et al., 2020; Tao et al., 2020;
 507 Witek et al., 2019) and the product is more intuitive and easier to use than previous versions.
 508 The product is available within 2 days from satellite overpass as a FIRSTLOOK version, and
 509 within 3-to-6 months as a final science-quality SA version that employs the most up-to-date

510 ancillary datasets. In response to the needs of operational user communities, a new MISR L2
511 NRT aerosol product has been developed with a 3-hour latency.

512 The new NRT algorithm does not depend on the upstream cloud classifiers that are
513 generated in L1 and L2 cloud processing. The lack of cloud classifiers is in large part mitigated
514 by the aerosol algorithm's built-in cloud identification methods. Analysis of the prototype NRT
515 product has shown an increased frequency of high-AOD retrievals, especially over oceans and
516 in climatologically cloudy areas, likely due to an increase in cloud contamination. Adjusting the
517 ARCI threshold in DW retrievals proves highly effective at eliminating some of these high-AOD
518 outliers and improves the NRT product's statistical agreement with the SA version. The new
519 NRT aerosol product applies an ARCI threshold of 0.18 to mitigate cloud contamination in the
520 absence of upstream cloud masks in NRT processing. The remaining differences in statistical
521 and geographic distributions between the NRT and SA AODs, which includes information from
522 the L2 cloud product, are small and largely confined to areas with high cloud cover.

523 The results of this study also serve as an example of the effects of screening threshold
524 adjustments in MISR aerosol retrievals on AOD statistics and distributions. Researchers
525 interested in particular applications and/or specific geographic regions are encouraged to
526 experiment with their own threshold to achieve most optimal results. The NRT aerosol product
527 contains both the recommended product contained within the main science directory
528 "4.4_KM_PRODUCTS" that has the stricter ARCI threshold ($ARCI \geq 0.18$), and the unscreened
529 product without the additional cloud and ARCI filtering designed for more experienced users,
530 located within the AUXILIARY group.

531

532 **Acknowledgements**

533 This research was carried out at the Jet Propulsion Laboratory, California Institute of
534 Technology, under a contract with the National Aeronautics and Space Administration. Support
535 from the MISR project is acknowledged. Special thanks to Andrew Sayer, [Jeffrey Reid](#), and one
536 anonymous reviewer for carefully reading the manuscript and providing valuable comments.

537

538 **Data availability**

539 The MISR V23 SA and NRT data is publicly available and can be downloaded from
540 <https://l0dup05.larc.nasa.gov/cgi-bin/MISR/main.cgi>. MISR NRT data is not stored permanently
541 and is only available for three to six months from the time of acquisition; please contact the
542 corresponding author to request the NRT data from the months analyzed in this study.

543 **References:**

- 544 Ackerman, S., Richard, F., Kathleen, S., Yinghui, L., Liam, G., Bryan, B. and Paul, M.:
545 Discriminating clear-sky from cloud with MODIS algorithm theoretical basis document
546 (MOD35), Univ. Wisconsin - Madison, 6th Edn.(October), 129 [online] Available from:
547 <http://citeseerx.ist.psu.edu/viewdoc/summary?doi=10.1.1.385.4885>, 2010.
- 548 Benedetti, A., Reid, J. S. and Colarco, P. R.: International cooperative for aerosol prediction
549 workshop on aerosol forecast verification, in *Bulletin of the American Meteorological Society*,
550 vol. 92., 2011.
- 551 Benedetti, A., Reid, J. S., Knippertz, P., Marsham, J. H., Di Giuseppe, F., Rémy, S., Basart, S.,
552 Boucher, O., Brooks, I. M., Menut, L., Mona, L., Laj, P., Pappalardo, G., Wiedensohler, A.,
553 Baklanov, A., Brooks, M., Colarco, P. R., Cuevas, E., Da Silva, A., Escribano, J., Flemming, J.,
554 Huneus, N., Jorba, O., Kazadzis, S., Kinne, S., Popp, T., Quinn, P. K., Sekiyama, T. T., Tanaka,
555 T. and Terradellas, E.: Status and future of numerical atmospheric aerosol prediction with a
556 focus on data requirements, *Atmos. Chem. Phys.*, 18, 10615–10643, doi:10.5194/acp-18-10615-
557 2018, 2018.
- 558 Bocquet, M., Elbern, H., Eskes, H., Hirtl, M., Aabkar, R., Carmichael, G. R., Flemming, J.,
559 Inness, A., Pagowski, M., Pérez Camaño, J. L., Saide, P. E., San Jose, R., Sofiev, M., Vira, J.,
560 Baklanov, A., Carnevale, C., Grell, G. and Seigneur, C.: Data assimilation in atmospheric
561 chemistry models: Current status and future prospects for coupled chemistry meteorology
562 models, *Atmos. Chem. Phys.*, 15(10), 5325–5358, doi:10.5194/acp-15-5325-2015, 2015.
- 563 Buchard, V., Da Silva, A. M., Colarco, P. R., Darmenov, A., Randles, C. A., Govindaraju, R.,
564 Torres, O., Campbell, J. and Spurr, R.: Using the OMI aerosol index and absorption aerosol
565 optical depth to evaluate the NASA MERRA Aerosol Reanalysis, *Atmos. Chem. Phys.*, 15(10),
566 5743–5760, doi:10.5194/acp-15-5743-2015, 2015.
- 567 Buchard, V., Randles, C. A., da Silva, A. M., Darmenov, A., Colarco, P. R., Govindaraju, R.,
568 Ferrare, R., Hair, J., Beyersdorf, A. J., Ziemba, L. D. and Yu, H.: The MERRA-2 aerosol
569 reanalysis, 1980 onward. Part II: Evaluation and case studies, *J. Clim.*, 30(17),
570 doi:10.1175/JCLI-D-16-0613.1, 2017.

571 Butz, A., Hasekamp, O. P., Frankenberg, C. and Aben, U.: Retrievals of atmospheric CO₂ from
572 simulated space-borne measurements of backscattered near-infrared sunlight: Accounting for
573 aerosol effects, *Appl. Opt.*, 48, 3322–3336, doi:10.1364/AO.48.003322, 2009.

574 Choi, M., Lim, H., Kim, J., Lee, S., Eck, T. F., Holben, B. N., Garay, M. J., Hyer, E. J., Saide, P.
575 E. and Liu, H.: Validation, comparison, and integration of GOCI, AHI, MODIS, MISR, and
576 VIIRS aerosol optical depth over East Asia during the 2016 KORUS-AQ campaign, *Atmos.*
577 *Meas. Tech.*, 12(8), 4619–4641, doi:10.5194/amt-12-4619-2019, 2019.

578 Colarco, P., Da Silva, A., Chin, M. and Diehl, T.: Online simulations of global aerosol
579 distributions in the NASA GEOS-4 model and comparisons to satellite and ground-based aerosol
580 optical depth, *J. Geophys. Res. Atmos.*, 115(14), doi:10.1029/2009JD012820, 2010.

581 Diner, D. J., Beckert, J. C., Reilly, T. H., Bruegge, C. J., Conel, J. E., Kahn, R. A., Martonchik,
582 J. V., Ackerman, T. P., Davies, R., Gerstl, S. A. W., Gordon, H. R., Muller, J. P., Myneni, R. B.,
583 Sellers, P. J., Pinty, B. and Verstraete, M. M.: Multiangle Image Spectroradiometer (MISR)
584 instrument description and experiment overview, *IEEE Trans. Geosci. Remote Sens.*, 36(4),
585 1072–1087, 1998.

586 Diner, D. J., Di Girolamo, L. and Clothiaux, E. E.: Level 1 Cloud Detection Algorithm
587 Theoretical Basis, *Jet Propuls. Lab. Calif. Inst. Technol.*, D-13397(Rev. B), 1999a.

588 Diner, D. J., Davies, R., Di Girolamo, L., Horvath, A., Moroney, C., Muller, J. P., Paradise, S.
589 R., Wenkert, D. and Zong, J.: Level 2 Cloud Detection and Classification Algorithm Theoretical
590 Basis, *Jet Propuls. Lab. Calif. Inst. Technol.*, D-11399(Rev. D), 1999b.

591 Diner, D. J., Abdou, W. A., Ackerman, T. P., Crean, K., Gordon, H. R., Kahn, R. A.,
592 Martonchik, J. V., McMuldroy, S., Paradise, S. R. and Pinty, B.: Level 2 aerosol retrieval
593 algorithm theoretical basis, *Jet Propuls. Lab. Calif. Inst. Technol.*, D-11400(Rev. G), 2008.

594 Frankenberg, C., Hasekamp, O., O'Dell, C., Sanghavi, S., Butz, A. and Worden, J.: Aerosol
595 information content analysis of multi-angle high spectral resolution measurements and its benefit
596 for high accuracy greenhouse gas retrievals, *Atmos. Meas. Tech.*, 5(7), 1809–1821,
597 doi:10.5194/amt-5-1809-2012, 2012.

598 Frouin, R. J., Franz, B. A., Ibrahim, A., Knobelspiesse, K., Ahmad, Z., Cairns, B., Chowdhary,
599 J., Dierssen, H. M., Tan, J., Dubovik, O., Huang, X., Davis, A. B., Kalashnikova, O., Thompson,
600 D. R., Remer, L. A., Boss, E., Coddington, O., Deschamps, P. Y., Gao, B. C., Gross, L.,
601 Hasekamp, O., Omar, A., Pelletier, B., Ramon, D., Steinmetz, F. and Zhai, P. W.: Atmospheric
602 Correction of Satellite Ocean-Color Imagery During the PACE Era, *Front. Earth Sci.*, 7,
603 doi:10.3389/feart.2019.00145, 2019.

604 Fu, G., Prata, F., Xiang Lin, H., Heemink, A., Segers, A. and Lu, S.: Data assimilation for
605 volcanic ash plumes using a satellite observational operator: A case study on the 2010
606 Eyjafjallajökull volcanic eruption, *Atmos. Chem. Phys.*, 17(2), 1187–1205, doi:10.5194/acp-17-
607 1187-2017, 2017.

608 Gao, B. C., Goetz, A. F. H. and Wiscombe, W. J.: Cirrus cloud detection from Airborne Imaging
609 Spectrometer data using the 1.38 μm water vapor band, *Geophys. Res. Lett.*, 20(3), 301–304,
610 doi:10.1029/93GL00106, 1993.

611 Garay, M. J., Witek, M. L., Kahn, R. A., Seidel, F. C., Limbacher, J. A., Bull, M. A., Diner, D.
612 J., Hansen, E. G. E. G., Kalashnikova, O. V., Lee, H., Nastan, A. M. and Yu, Y.: Introducing the
613 4.4km spatial resolution Multi-Angle Imaging SpectroRadiometer (MISR) aerosol product,
614 *Atmos. Meas. Tech.*, 13(2), 593–628, doi:10.5194/amt-13-593-2020, 2020.

615 Gelaro, R., McCarty, W., Suárez, M. J., Todling, R., Molod, A., Takacs, L., Randles, C. A.,
616 Darnenov, A., Bosilovich, M. G., Reichle, R., Wargan, K., Coy, L., Cullather, R., Draper, C.,
617 Akella, S., Buchard, V., Conaty, A., da Silva, A. M., Gu, W., Kim, G. K., Koster, R., Lucchesi,
618 R., Merkova, D., Nielsen, J. E., Partyka, G., Pawson, S., Putman, W., Rienecker, M., Schubert,
619 S. D., Sienkiewicz, M. and Zhao, B.: The modern-era retrospective analysis for research and
620 applications, version 2 (MERRA-2), *J. Clim.*, 30(14), 5419–5454, doi:10.1175/JCLI-D-16-
621 0758.1, 2017.

622 Girolamo, L. Di and Davies, R.: A Band-Differenced Angular Signature Technique for Cirrus
623 Cloud Detection, *IEEE Trans. Geosci. Remote Sens.*, 32(4), 890–896, doi:10.1109/36.298017,
624 1994.

625 Girolamo, L. Di and Davies, R.: The Image Navigation Cloud Mask for the Multiangle Imaging

626 Spectroradiometer (MISR), *J. Atmos. Ocean. Technol.*, 12(6), doi:10.1175/1520-
627 0426(1995)012<1215:tinmf>2.0.co;2, 1995.

628 Gordon, R.: Atmospheric correction of ocean color imagery in the Earth Observing System era,
629 *J. Geophys. Res. - Atmos.*, 102(D14), 17081–17106, doi:10.1029/96JD02443, 1997.

630 Houweling, S., Hartmann, W., Aben, I., Schrijver, H., Skidmore, J., Roelofs, G. J. and Breon, F.
631 M.: Evidence of systematic errors in SCIAMACHY-observed CO₂ due to aerosols, *Atmos.*
632 *Chem. Phys.*, 5(11), 3003–3013, doi:10.5194/acp-5-3003-2005, 2005.

633 Inness, A., Baier, F., Benedetti, A., Bouarar, I., Chabrilat, S., Clark, H., Clerbaux, C., Coheur,
634 P., Engelen, R. J., Errera, Q., Flemming, J., George, M., Granier, C., Hadji-Lazaro, J., Huijnen,
635 V., Hurtmans, D., Jones, L., Kaiser, J. W., Kapsomenakis, J., Lefever, K., Leitão, J., Razinger,
636 M., Richter, A., Schultz, M. G., Simmons, A. J., Suttie, M., Stein, O., Thépaut, J. N., Thouret,
637 V., Vrekoussis, M. and Zerefos, C.: The MACC reanalysis: An 8 yr data set of atmospheric
638 composition, *Atmos. Chem. Phys.*, 13(8), 4073–4109, doi:10.5194/acp-13-4073-2013, 2013.

639 Inness, A., Ades, M., Agustí-Panareda, A., Barré, J., Benedictow, A., Blechschmidt, A.-M.,
640 Dominguez, J. J., Engelen, R., Eskes, H., Flemming, J., Huijnen, V., Jones, L., Kipling, Z.,
641 Massart, S., Parrington, M., Peuch, V.-H., Razinger, M., Remy, S., Schulz, M. and Suttie, M.:
642 The CAMS reanalysis of atmospheric composition, *Atmos. Chem. Phys.*, 19(6), 3515–3556,
643 doi:10.5194/acp-19-3515-2019, 2019.

644 IPCC: Climate Change 2013: The Physical Science Basis. Contribution of Working Group I to
645 the Fifth Assessment Report of the Intergovernmental Panel on Climate Change, edited by T. F.
646 Stocker, D. Qin, G. K. Plattner, M. M. B. Tignor, S. K. Allen, J. Boschung, A. Nauels, Y. Xia,
647 V. Bex, and P. M. Midgley, Cambridge University Press, Cambridge, United Kingdom and New
648 York, NY, USA., 2013.

649 Kahn, R. A. and Gaitley, B. J.: An analysis of global aerosol type as retrieved by MISR, *J.*
650 *Geophys. Res. Atmos.*, 120(9), 4248–4281, doi:10.1002/2015JD023322, 2015.

651 Kahn, R. A., Gaitley, B. J., Garay, M. J., Diner, D. J., Eck, T. F., Smirnov, A. and Holben, B. N.:
652 Multiangle Imaging SpectroRadiometer global aerosol product assessment by comparison with

653 the Aerosol Robotic Network, *J. Geophys. Res. Atmos.*, 115(23), doi:10.1029/2010JD014601,
654 2010.

655 Kalashnikova, O. V., Garay, M. J., Martonchik, J. V. and Diner, D. J.: MISR Dark Water aerosol
656 retrievals: Operational algorithm sensitivity to particle non-sphericity, *Atmos. Meas. Tech.*, 6(8),
657 2131–2154, doi:10.5194/amt-6-2131-2013, 2013.

658 Lamarque, J. F., Shindell, D. T., Josse, B., Young, P. J., Cionni, I., Eyring, V., Bergmann, D.,
659 Cameron-Smith, P., Collins, W. J., Doherty, R., Dalsoren, S., Faluvegi, G., Folberth, G., Ghan,
660 S. J., Horowitz, L. W., Lee, Y. H., MacKenzie, I. A., Nagashima, T., Naik, V., Plummer, D.,
661 Righi, M., Rumbold, S. T., Schulz, M., Skeie, R. B., Stevenson, D. S., Strode, S., Sudo, K.,
662 Szopa, S., Voulgarakis, A. and Zeng, G.: The atmospheric chemistry and climate model
663 intercomparison Project (ACCMIP): Overview and description of models, simulations and
664 climate diagnostics, *Geosci. Model Dev.*, 6(1), 179–206, doi:10.5194/gmd-6-179-2013, 2013.

665 Lelieveld, J., Evans, J. S., Fnais, M., Giannadaki, D. and Pozzer, A.: The contribution of outdoor
666 air pollution sources to premature mortality on a global scale, *Nature*, 525(7569), 367–371,
667 doi:10.1038/nature15371, 2015.

668 Levy, R. C., Mattoo, S., Munchak, L. A., Remer, L. A., Sayer, A. M., Patadia, F. and Hsu, N. C.:
669 The Collection 6 MODIS aerosol products over land and ocean, *Atmos. Meas. Tech.*, 6(11),
670 2989–3034, doi:10.5194/amt-6-2989-2013, 2013.

671 Liu, M., Westphal, D. L., Walker, A. L., Holt, T. R., Richardson, K. A. and Miller, S. D.:
672 COAMPS real-time dust storm forecasting during operation Iraqi freedom, *Weather Forecast.*,
673 22(1), 192–206, doi:10.1175/WAF971.1, 2007.

674 Lynch, P., Reid, J. S., Westphal, D. L., Zhang, J., Hogan, T. F., Hyer, E. J., Curtis, C. A., Hegg,
675 D. A., Shi, Y., Campbell, J. R., Rubin, J. I., Sessions, W. R., Turk, F. J. and Walker, A. L.: An
676 11-year global gridded aerosol optical thickness reanalysis (v1.0) for atmospheric and climate
677 sciences, *Geosci. Model Dev.*, 9(4), 1489–1522, doi:10.5194/gmd-9-1489-2016, 2016.

678 Martonchik, J. V., Kahn, R. A. and Diner, D. J.: Retrieval of aerosol properties over land using
679 MISR observations, in *Satellite Aerosol Remote Sensing over Land*, pp. 267–293, Springer

680 Berlin Heidelberg., 2009.

681 Randles, C. A., da Silva, A. M., Buchard, V., Colarco, P. R., Darmenov, A., Govindaraju, R.,
682 Smirnov, A., Holben, B., Ferrare, R., Hair, J., Shinozuka, Y. and Flynn, C. J.: The MERRA-2
683 aerosol reanalysis, 1980 onward. Part I: System description and data assimilation evaluation, *J.*
684 *Clim.*, 30(17), 6823–6850, doi:10.1175/JCLI-D-16-0609.1, 2017.

685 Reid, J. S., Benedetti, A., Colarco, P. R. and Hansen, J. A.: International operational aerosol
686 observability workshop, in *Bulletin of the American Meteorological Society*, vol. 92., 2011.

687 Rienecker, M. M., Suarez, M. J., Gelaro, R., Todling, R., Bacmeister, J., Liu, E., Bosilovich, M.
688 G., Schubert, S. D., Takacs, L., Kim, G. K., Bloom, S., Chen, J., Collins, D., Conaty, A., Da
689 Silva, A., Gu, W., Joiner, J., Koster, R. D., Lucchesi, R., Molod, A., Owens, T., Pawson, S.,
690 Pegion, P., Redder, C. R., Reichle, R., Robertson, F. R., Ruddick, A. G., Sienkiewicz, M. and
691 Woollen, J.: MERRA: NASA’s modern-era retrospective analysis for research and applications,
692 *J. Clim.*, 24, 3624–3648, doi:10.1175/JCLI-D-11-00015.1, 2011.

693 Sayer, A. M. and Knobelspiesse, K. D.: How should we aggregate data? Methods accounting for
694 the numerical distributions, with an assessment of aerosol optical depth, *Atmos. Chem. Phys.*,
695 19(23), 15023–15048, doi:10.5194/acp-19-15023-2019, 2019.

696 Sayer, A. M., Govaerts, Y., Kolmonen, P., Lipponen, A., Luffarelli, M., Mielonen, T., Patadia,
697 F., Popp, T., Povey, A. C., Stebel, K. and Witek, M. L.: A review and framework for the
698 evaluation of pixel-level uncertainty estimates in satellite aerosol remote sensing, *Atmos. Meas.*
699 *Tech.*, 13(2), 373–404, doi:10.5194/amt-13-373-2020, 2020.

700 Sekiyama, T. T., Tanaka, T. Y., Shimizu, A. and Miyoshi, T.: Data assimilation of CALIPSO
701 aerosol observations, *Atmos. Chem. Phys.*, 10(1), 39–49, doi:10.5194/acp-10-39-2010, 2010.

702 Shi, Y., Zhang, J., Reid, J. S., Holben, B., Hyer, E. J. and Curtis, C.: An analysis of the collection
703 5 MODIS over-ocean aerosol optical depth product for its implication in aerosol assimilation,
704 *Atmos. Chem. Phys.*, 11(2), 557–565, doi:10.5194/acp-11-557-2011, 2011.

705 Shi, Y., Zhang, J., Reid, J. S., Hyer, E. J. and Hsu, N. C.: Critical evaluation of the MODIS Deep
706 Blue aerosol optical depth product for data assimilation over North Africa, *Atmos. Meas. Tech.*,

707 6(4), 949–969, doi:10.5194/amt-6-949-2013, 2013.

708 Shi, Y., Zhang, J., Reid, J. S., Liu, B. and Hyer, E. J.: Critical evaluation of cloud contamination
709 in the MISR aerosol products using MODIS cloud mask products, *Atmos. Meas. Tech.*, 7(6),
710 1791–1801, doi:10.5194/amt-7-1791-2014, 2014.

711 Shindell, D. T., Lamarque, J. F., Schulz, M., Flanner, M., Jiao, C., Chin, M., Young, P. J., Lee,
712 Y. H., Rotstayn, L., Mahowald, N., Milly, G., Faluvegi, G., Balkanski, Y., Collins, W. J.,
713 Conley, A. J., Dalsoren, S., Easter, R., Ghan, S., Horowitz, L., Liu, X., Myhre, G., Nagashima,
714 T., Naik, V., Rumbold, S. T., Skeie, R., Sudo, K., Szopa, S., Takemura, T., Voulgarakis, A.,
715 Yoon, J. H. and Lo, F.: Radiative forcing in the ACCMIP historical and future climate
716 simulations, *Atmos. Chem. Phys.*, 13(6), 2939–2974, doi:10.5194/acp-13-2939-2013, 2013.

717 Si, Y., Chen, L., Xiong, X., Shi, S., Husi, L. and Cai, K.: Evaluation of the MISR fine resolution
718 aerosol product using MODIS, MISR, and ground observations over China, *Atmos. Environ.*,
719 223(December 2019), 117229, doi:10.1016/j.atmosenv.2019.117229, 2020.

720 Sogacheva, L., Popp, T., Sayer, A. M., Dubovik, O., Garay, M. J., Heckel, A., Hsu, N. C.,
721 Jethva, H., Kahn, R. A., Kolmonen, P., Kosmale, M., de Leeuw, G., Levy, R. C., Litvinov, P.,
722 Lyapustin, A., North, P., Torres, O. and Arola, A.: Merging regional and global aerosol optical
723 depth records from major available satellite products, *Atmos. Chem. Phys.*, 20(4), 2031–2056,
724 doi:10.5194/acp-20-2031-2020, 2020.

725 Tao, M., Wang, J., Li, R., Chen, L., Xu, X., Wang, L., Tao, J., Wang, Z. and Xiang, J.:
726 Characterization of Aerosol Type Over East Asia by 4.4 km MISR Product: First Insight and
727 General Performance, *J. Geophys. Res. Atmos.*, 125(13), 1–16, doi:10.1029/2019JD031909,
728 2020.

729 Di Tomaso, E., Schutgens, N. A. J., Jorba, O. and García-Pando, C. P.: Assimilation of MODIS
730 Dark Target and Deep Blue observations in the dust aerosol component of NMMB-MONARCH
731 version 1.0, *Geosci. Model Dev.*, 10(3), 1107–1129, doi:10.5194/gmd-10-1107-2017, 2017.

732 Turnock, S. T., Allen, R. J., Andrews, M., Bauer, S. E., Deushi, M., Emmons, L., Good, P.,
733 Horowitz, L., John, J. G., Michou, M., Nabat, P., Naik, V., Neubauer, D., O’Connor, F. M.,

734 Olivić, D., Oshima, N., Schulz, M., Sellar, A., Shim, S., Takemura, T., Tilmes, S., Tsigaridis, K.,
735 Wu, T. and Zhang, J.: Historical and future changes in air pollutants from CMIP6 models,
736 *Atmos. Chem. Phys.*, 20(23), 14547–14579, doi:10.5194/acp-20-14547-2020, 2020.

737 Werner, M., Kryza, M. and Guzikowski, J.: Can data assimilation of surface PM_{2.5} and Satellite
738 AOD improve WRF-Chem Forecasting? A case study for two scenarios of particulate air
739 pollution episodes in Poland, *Remote Sens.*, 11(20), doi:10.3390/rs11202364, 2019.

740 Witek, M. L., Garay, M. J., Diner, D. J. and Smirnov, A.: Aerosol optical depths over oceans: A
741 view from MISR retrievals and collocated MAN and AERONET in situ observations, *J.*
742 *Geophys. Res. Atmos.*, 118(22), 12620–12633, doi:10.1002/2013JD020393, 2013.

743 Witek, M. L., Diner, D. J., Garay, M. J., Xu, F., Bull, M. A. and Seidel, F. C.: Improving MISR
744 AOD Retrievals with Low-Light-Level Corrections for Veiling Light, *IEEE Trans. Geosci.*
745 *Remote Sens.*, 56(3), 1251–1268, doi:10.1109/TGRS.2017.2727342, 2018a.

746 Witek, M. L., Garay, M. J., Diner, D. J., Bull, M. A. and Seidel, F. C.: New approach to the
747 retrieval of AOD and its uncertainty from MISR observations over dark water, *Atmos. Meas.*
748 *Tech.*, 11(1), 429–439, doi:10.5194/amt-11-429-2018, 2018b.

749 Witek, M. L., Garay, M. J., Diner, D. J. and Smirnov, A.: Oceanic Aerosol Loading Derived
750 From MISR's 4.4 km (V23) Aerosol Product, *J. Geophys. Res. Atmos.*, 124(17–18), 10154–
751 10174, doi:10.1029/2019JD031065, 2019.

752 Xian, P., Reid, J. S., Hyer, E. J., Sampson, C. R., Rubin, J. I., Ades, M., Asencio, N., Basart, S.,
753 Benedetti, A., Bhattacharjee, P. S., Brooks, M. E., Colarco, P. R., da Silva, A. M., Eck, T. F.,
754 Guth, J., Jorba, O., Kouznetsov, R., Kipling, Z., Sofiev, M., Perez Garcia-Pando, C., Pradhan,
755 Y., Tanaka, T., Wang, J., Westphal, D. L., Yumimoto, K. and Zhang, J.: Current state of the
756 global operational aerosol multi-model ensemble: An update from the International Cooperative
757 for Aerosol Prediction (ICAP), *Q. J. R. Meteorol. Soc.*, 145, 176–209, doi:10.1002/qj.3497,
758 2019.

759 Zhang, J. and Reid, J. S.: An analysis of clear sky and contextual biases using an operational
760 over ocean MODIS aerosol product, *Geophys. Res. Lett.*, 36(15), doi:10.1029/2009GL038723,

761 2009.

762 Zhang, J. and Reid, J. S.: A decadal regional and global trend analysis of the aerosol optical
763 depth using a data-assimilation grade over-water MODIS and Level 2 MISR aerosol products,
764 *Atmos. Chem. Phys.*, 10(22), 10949–10963, doi:10.5194/acp-10-10949-2010, 2010.

765 Zhang, J., Reid, J. S., Westphal, D. L., Baker, N. L. and Hyer, E. J.: A system for operational
766 aerosol optical depth data assimilation over global oceans, *J. Geophys. Res. Atmos.*, 113(10), 1–
767 13, doi:10.1029/2007JD009065, 2008.

768